VCSEL Quick Fabrication for Assessment of Large Diameter Epitaxial Wafers

Jack Baker, *Graduate Student Member, IEEE*, Sara Gillgrass, Craig P. Allford, Tomas Peach, Curtis Hentschel, Tracy Sweet, J. Iwan Davies, Samuel Shutts, and Peter M. Smowton, *Senior Member, IEEE*

***Abstract*—Stripped-back representative VCSEL devices with a simple fabrication process that very closely approaches the performance of standard BCB-planarised devices have been produced. These VCSEL Quick Fabrication (VQF) devices achieve threshold currents only 0.3 mA higher than that of a standard device produced from the same material. The predictability of standard performance from VQF performance is also robustly assessed in terms of temperature effects to account for the observed disparities. These VQF devices are then processed across a 6-inch (152 mm) wafer and the resulting device-level characteristics are mapped. From this, it is apparent that there is an approximately radial decrease in oxide aperture diameter from centre to edge, found to be driven by the strain-induced wafer bow. After corrections, a residual spatial variation across the wafer remains, which, in conjunction with temperature dependent measurements, is shown to be a result of epi-material variation. By observation at 50 °C, that is, at a temperature closely resembling that of intended application, the residual centre-to-edge variation in threshold current density is found to be only 0.2 kA/cm^2, compared to 1.3 kA/cm^2 when observing the room temperature variation of devices of nominally equivalent active volumes.**

***Index Terms*—Epitaxy, manufacturing, VCSEL, wafer.**

I. Introduction

In RECENT years, vertical-cavity surface-emitting laser (VCSEL) epi-wafer manufacturers have scaled up production to large diameter substrates to meet a growing demand, whilst advanced applications are requiring tighter specifications and tolerances. This heightens the importance of maintaining quality and uniformity throughout manufacturing processes, which increases the need for rapid fabrication of devices on sacrificial material for enhanced characterisation and for tracking drift during a growth campaign. Variation in the epitaxial layers over large diameter wafers can be significant, and, in the context of maximising manufacturing yield, existing wafer characterisation needs to be complemented with measurement of real devices without significant impact on production. However, this is often a time-consuming process incompatible with the environment of high-volume manufacture. Therefore, there is a need for a method of rapid production of simplified, but representative, VCSEL devices, the characterisation of which can be used to feedback to growth conditions.

One of the most attractive features of surface-emitting lasers is the ease of fabrication, although, it is not without its complications. The electrical and optical confinement afforded by the use of selective oxidation of high-Al composition AlGaAs layers led to a marked improvement in the performance of VCSELs [1]–[3]. The confinement layers, which are buried within the epitaxial structure, must be exposed prior to oxidation by etching, which results in non-planarity. Early on, this challenge was overcome by subsequently planarising the VCSEL mesa using polyimide [4], [5], and, since then, benzocyclobutene (BCB) [6], [7]. This need for planarity adds complexity to the fabrication process and there have been attempts to produce planar VCSELs by utilising the electrical isolation provided by the oxidation process. One approach, used in [8], produces an array of individually addressable oxide confined VCSELs. The performance of these devices is both electrically and optically uniform, although a high open-area aspect ratio etch combined with a deep oxidation is required for simultaneous definition of the laser aperture and electrical isolation of the contact pad. In [9] and [10], via holes are etched to expose the high Al-content oxidation layer for definition of the VCSEL aperture/isolation of the contact pad, however, in both cases ion-implantation is also required. A high-density VCSEL array is produced in [11] by selective oxidation, with the apertures defined by a hexagonal grid of etched via holes, although this process requires a transparent p-metal. Definition of the VCSEL mesa by continuous and non-continuous ring trench etching is studied in [12] and it is shown that favourable thermal properties can be achieved. However, with this design there is still the need for deposition of a dielectric layer to electrically isolate the interconnect and

Manuscript received January 24, 2022; revised April 12, 2022; accepted April 15, 2022. Date of publication April 22, 2022; date of current version May 20, 2022. This work was supported in part by the Future Compound Semiconductor Manufacturing Hub, in part by the Engineering and Physical Sciences Research Council (EPSRC) Future Compound Semiconductor Manufacturing Hub, under Grant EP/P006973/1, in part by an EPSRC-funded iCASE PhD studentship supported by IQE plc. under Grant EP/T517525/1, in part by the EPSRC-funded iCASE Ph.D. studentship, in part by IQE plc. under Grant EP/T517525/1, in part by European Regional Development Fund through SMART Expertise Project ATLAS under Grant 82371, and in part by the Strength in Places Fund under Project 107134. *(Corresponding author: Jack Baker.)*

Jack Baker and Curtis Hentschel are with the Future Compound Semiconductor Manufacturing Hub, Cardiff University, Cardiff CF24 3AA, U.K., and also with the IQE plc, Cardiff CF3 0LW, U.K. (e-mail: bakerj19@cardiff.ac.uk; hentschelct@cardiff.ac.uk).

Sara Gillgrass, Craig P. Allford, and Samuel Shutts are with the Future Compound Semiconductor Manufacturing Hub, Cardiff University, Cardiff CF24 3AA, U.K. (e-mail: gillgrasss@cardiff.ac.uk; allfordcp1@cardiff.ac.uk; shuttss@cardiff.ac.uk).

Tomas Peach is with the Institute for Compound Semiconductors, Cardiff University, Cardiff CF24 3AA, U.K. (e-mail: peacht@cardiff.ac.uk).

Tracy Sweet and J. Iwan Davies are with the IQE plc, Cardiff CF3 0LW, U.K. (e-mail: tracysweet@iqep.com; idavies@iqep.com).

Peter M. Smowton is with the Future Compound Semiconductor Manufacturing Hub and the Institute for Compound Semiconductors, Cardiff University, Cardiff CF24 3AA, U.K. (e-mail: smowtonpm@cardiff.ac.uk).

Digital Object Identifier 10.1109/JPHOT.2022.3169032

contact pad. In this work, a method to rapidly produce VCSEL devices is developed which employs similar principles.

In commercialised VCSELs, the epitaxial structure most often employs a λ-thick inner cavity containing a multiple quantum well (MQW) active region sandwiched between two distributed Bragg reflector (DBR) mirrors, and it is this basic make-up of a VCSEL which is considered here. The dip in the reflectivity spectrum resulting from this structure means that VCSELs intrinsically operate as single longitudinal mode, with the lasing wavelength determined by the longitudinal cavity resonance. As such reflectometry measurements are utilised to characterise VCSEL epi-material, with the wavelength of the dip in the stopband used to predict the emission wavelength of a fabricated device [13]. Although, the resulting VCSEL devices operate with a red-shifted lasing wavelength due to the thermo-optic effect, with the magnitude of the redshift dependent on the extent of Joule heating [14], [15].

The small active volume of VCSELs results in low threshold currents, I_{th}, which continue to decrease with further reduction in lateral dimensions until the optical losses due to scattering and diffraction increase in very small devices [16], [17], driving an increase in threshold current density, J_{th}. At larger aperture diameters J_{th} becomes an approximately constant value [18]. Additionally, for VCSELs with exposed mesa sidewalls, dangling bonds give rise to surface states which provide a non-radiative recombination path for carriers [19], [20]. The rate of surface recombination can be reduced by passivating the sidewalls with a dielectric, such as BCB, however, in either case, the fractional change in surface recombination rate increases as the lateral dimensions of the device are reduced. Hence devices with active diameters 10 μm are targeted to maximise uniformity across a wafer.

Furthermore, given that the lasing wavelength is determined solely by the material cavity resonance, the VCSEL does not necessarily lase at the wavelength with the highest available gain [13], [21]. This, combined with the different temperature dependence of both the cavity resonance, λ_{cav}, [22] and gain peak wavelength, λ_{pk} , [23], results in there being an optimum temperature of operation for a VCSEL, that is, where these wavelengths align. The available gain at the material cavity resonance wavelength is greatest when there is zero detuning ($\Delta\lambda = \lambda_{pk} - \lambda_{cav}$), and this corresponds to a minimum threshold current density, J_{th}, which occurs at temperature T_{min} [24]–[26]. In a commercial setting, growth conditions are tailored to maximise the proportion of a wafer that results in low threshold performance; therefore, the gain peak-to-cavity resonance detuning is an important consideration, which can be probed though the characterisation of stripped-back VCSEL devices.

Here, a processing technique for VCSEL Quick Fabrication (VQF) is introduced and the performance of VQF devices is characterised. The devices rely on atypical geometries and the definition of oxidation-vias, such that both the electrical isolation of the contact pad and definition of the laser aperture are produced solely by selective oxidation of a buried high-Al layer, which results in a considerable reduction in processing time, although this is of course to the detriment of some performance characteristics, particularly the RF modulation bandwidth resulting from the non-ideal electrical parasitics. Characterisation methods are tailored to probe epitaxial material quality via VQF performance by assessing against the physical effects described in the introduction and by determining important device characteristics, such as threshold current, emission wavelength and gain peak detuning - which are important considerations in epi-design regardless of final device application. The oxide confined VQF devices that are produced reflect the behaviour of standard oxide confined VCSEL structures, with some physical limitations that are quantified here.

II. Methodology

A. Device Fabrication

The epitaxial structure of the VCSELs produced in this work are generic p-i-n layout, designed for 940 nm emission wavelength. This consists of a MQW gain medium sandwiched between upper p-doped AlGaAs/AlGaAs DBR and lower n-doped DBR comprising of both AlGaAs/AlGaAs and AlAs/AlGaAs mirrors pairs. One high Al-content layer is included between the active region and the upper DBR to act as current confinement/blocking layers after oxidation. The epitaxial material for the on-tile and full-wafer studies are nominally identical and were produced in the same growth run by IQE plc.

The fabrication of the standard structures produced in this study followed typical processing techniques for BCB-planarised VCSELs. Top p-metal ohmic contacts are formed by physical vapour deposition (PVD) of Ti/Pt/Au, which is done prior to the etch step. The VCSEL circular mesas are then formed using an inductively coupled plasma (ICP) etch to just below the active region. The laser aperture is defined by wet thermal oxidation, with a total oxidation length of $9.0\pm$ 0.5 μm measured in-situ using an infrared camera. Here, the uncertainty in the oxidation length is given as the resolution of the measurement. Spin-coating of BCB is then used to planarise the sample with a subsequent dry etch then required to open the VCSEL top surface. This is followed by deposition of Ti/Au contact pad and interconnect to the VCSEL ring contact. A back-side blanket-coat deposition of AuGe/Ni/Au provides a global n-contact metal, and this is followed by an annealing step.

In the context of this work, it is important that fabrication time is minimised, and therefore the VQF structure is designed to remove multiple, time-consuming processes. The entire fabrication can be broken down concisely into 7 steps: two lithography; two metallisation; single etch; oxidation and one annealing step. Initially, optical lithography is used to define the geometry of the structures which includes, in a departure from the full process, both the mesa and the contact pad regions. The structure is then etched to expose the high Al-content oxidation layers. Upon wet thermal oxidation, in addition to the aperture formation in the VCSEL mesa, via-holes are utilised to provide complete electrical isolation under the contact pads, ensuring that only the aperture region provides electrical conductivity through the junction. An oxidation length of 13.5 $\pm$ 0.5 μm sufficient to fully isolate the contact pad and generate the desired VCSEL

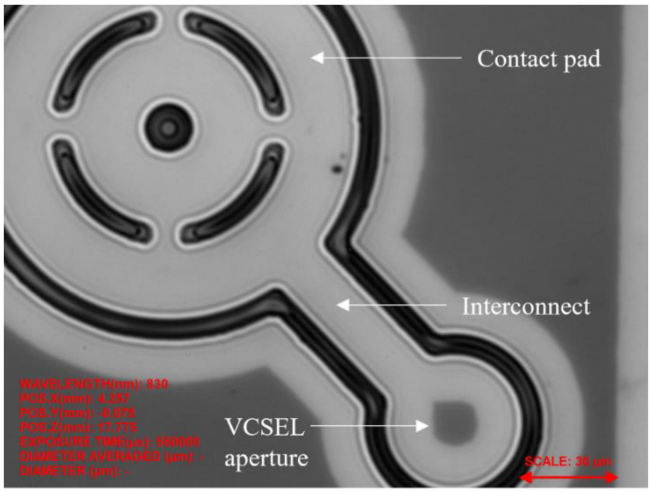

Fig. 1. Infrared camera image of oxidised VQF VCSEL structure, showing slightly non-circular aperture shape.

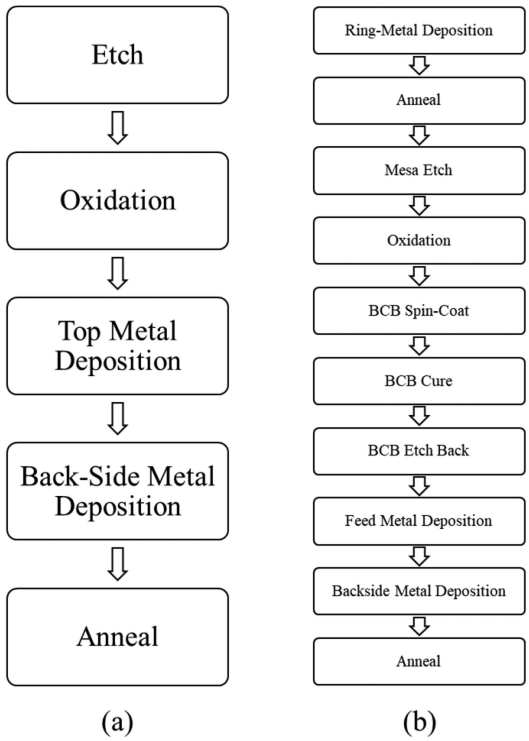

Fig. 2. Process flow for VQF (a) and standard VCSEL fabrication (b).

apertures. This length is intrinsically linked to the dimensions of the device design and therefore could be further reduced; however, this would increase the complexity of the subsequent lithography step and eventually result in a reduction in the overall device yield. The second lithography process is used to define the p-contact which is then deposited using Ti/Pt/Au PVD. The final two steps are a blanket backside AuGe/Ni/Au metallisation for a global n-contact and substrate annealing. The significant departures of the VQF process, from the previously described standard VCSEL, are the elimination of the requirement for BCB planarisation and the utilisation of only a single top-side metallisation step. Thus, the total fabrication time reduces by $\sim$ 60%. A top-view image of a VQF device after thermal oxidation is shown in Fig. 1. A slight non-circularity of the VCSEL aperture (due to the mesa-interconnect geometry) can also be seen in Fig. 1. The fabrication process for both device types is summarised in Fig. 2.

The initial study assessing various design variations was carried out on a single 12.5 $\times$ 12.5 mm tile to minimise the effect of epitaxial layer variation on device performance. The VCSELs were processed into groups of 10x10 arrays on a 250 μm pitch, with 16 groups per tile. Subsequently full-wafer fabrication involved patterning 96 tiles over a 6-inch (152 mm) wafer.

B. Experimental Procedure

Given the need for rapid feedback, the characterisation of these VCSELs is also streamlined to obtain valuable information which provides insight into epitaxial material variation but with a minimum time cost.

To mirror techniques used in industry, and to minimise the time-to-result for characterisation, light-current-voltage-wavelength (L-I-V-λ) measurements were performed on a semi-automatic wafer-prober equipped with an optical fibre for direct coupling of the laser emission. Whilst only allowing measurements of light output in arbitrary units, measurement of the current-voltage characteristic, lasing threshold current, and emission spectra were still possible.

After initial L-I-V-λ characterisation, the performance of the optimal VQF devices designs were compared to that of standard devices on an upgraded temperature-controlled wafer-probing setup, equipped with a calibrated integrating sphere for light collection. This setup was used for measuring temperature-dependent L-I-V characteristics from 20 to 70 °C and provided measurements of true output powers.

Measurement of the oxidation length at several locations on the wafer was carried out during processing using an infra-red camera. Additionally, samples were taken from the centre and edge of a nominally identical wafer and circular mesa structures were oxidised to assess the difference in oxidation length due to properties of the oxidation layers in the epitaxial structure.

III. Results and Discussion

A. On-Tile VQF Performance

First the relative performance of VQF and standard devices is considered. The devices were produced on 12.5 $\times$ 12.5 mm tiles of equivalent epitaxial material taken from the centre of a 152 mm wafer. An artifact arising from the difference in device geometry, is a difference in oxidation length required to define the oxide apertures. As such, definition of devices of precisely equivalent aperture diameters was not possible, and when comparing typical performance for each device type, the behaviour of larger aperture diameter devices (7 – 9 μm) is carried out to minimise the limitations associated with small aperture devices, for example error in oxide aperture diameter

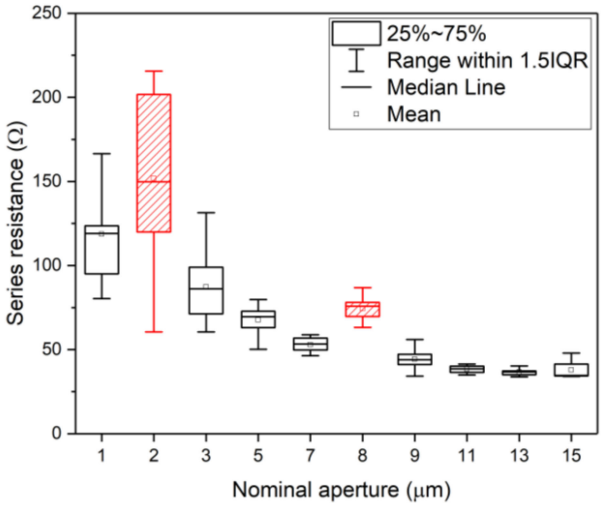

Fig. 3. Box and whisker plots of series resistance extracted from I-V characteristic (2.4-2.5 V) for a range of oxide apertures for both VQF (plain black boxes) and standard VCSEL devices (red striped boxes).

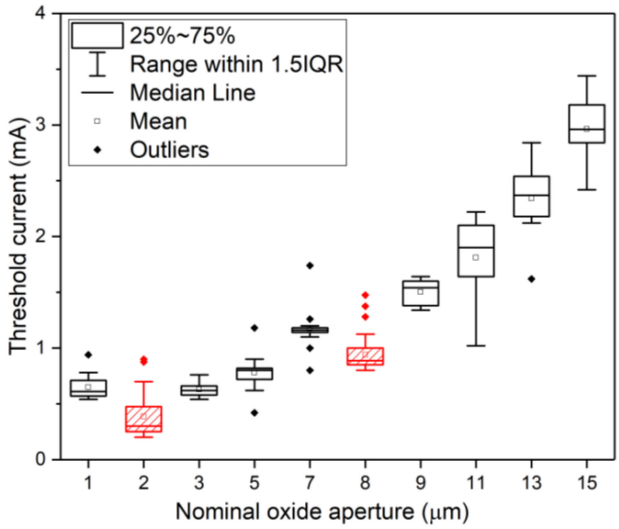

Fig. 4. Box and whisker plots of measured threshold current values for a range of oxide aperture diameters for both VQF (plain black boxes) and standard (red striped boxes) VCSEL devices.

and scattering loss. A comparison of the dependence on oxide aperture diameter of series resistance, extracted from the I-V characteristic between 2.4 and 2.5 V, is shown in Fig. 3, for both VQF and standard devices.

The mean series resistances of the standard VCSELs are found to be approximately 25 Ω higher than that of the VQF devices, and this difference is constant with aperture size, hence is likely systematic and associated with the difference in p-contact definition for both device types. For the standard VCSELs, there is a contact resistance related to the deposition of the feed metal onto the p-contact ring which is not present for the VQF devices given that the contact pad and feed metal are deposited simultaneously and directly onto semiconductor. Additionally, the thickness and width of the p-contact ring metal is less than that of the VQF devices, which also contributes to an increased series resistance. Further, although there is a slight difference in active area for nominally equal oxide apertures (due to the non-circularity of the VQF devices) the effect on series resistance should be small given that the VQF active area is only ∼7% larger. This higher series resistance of the standard VCSELs thus contributes to increased Joule heating in those devices and hence a higher internal temperature.

In Fig. 4, the dependence of threshold current on aperture diameter for both device types is shown. It can be seen that for the VQF VCSEL design we approach comparable performance for a stripped-back structure, achieving values of I_{th}, that closely match that of standard structures. However, a small increase of approximately 0.3 mA in the mean threshold current for the VQF devices relative to a standard device of similar active volume is observed. This difference can be shown, partly, to be a result of temperature effects associated with a difference in thermal mass of the VQF and standard structures, but there are additional contributions which are also considered.

The temperature dependence of I_{th} was measured for a range of apertures for both standard and VQF devices, some of which are shown in Fig. 5 (top). Based on the same analysis as in [27], we extract from these plots the threshold current minimum, α, and the temperature at which the threshold current minimum occurs, $\mathrm{T_{min}}$. This minimum is observed to occur at approximately 45 °C and there is a small variation (±5 °C) for all the devices measured, whether standard or VQF designs, hence, the gain peak-to-cavity resonance detuning is very similar both device types. In addition to a higher series resistance, the standard VCSELs have increased thermal impedances due to the deeper oxidation lengths for the VQF devices. Hence, for equivalent active areas, the thermal impedance of a standard VCSEL is higher than that of a VQF device, and the standard VCSEL operates at higher internal temperatures for a given current. Thus, by considering Fig. 5 (top), at ambient room temperature, the standard VCSELs operate closer to $\mathrm{T_{min}}$ due to extra internal heating, which results in a greater decrease in threshold current relative to VQF devices.

Additionally, it is likely that there is an increased rate of surface recombination at the exposed mesa sidewalls of the VQF devices relative to the BCB-passivated standard devices, which contributes to a higher threshold current [28]. Also, as seen in Fig. 1, the VQF device design results in slightly non-circular aperture shapes, owing to the interconnect region of the device, which increases the active area by ∼7% relative to the circular aperture of a standard device. Given that the threshold current of a VCSEL scales with active volume, this also contributes to increase in threshold current for VQF relative to a standard device.

Further, it is possible that variation in the epitaxial layers may also contribute to a difference in threshold current. Separate to the effect of gain peak-to-cavity resonance detuning, spatial variation in material composition and layer thickness of the DBR layers impacts the mirror reflectivity, which is intimately linked to the threshold gain [19], [29]. However, the effect of epi-layer variation should be small on tile-sized samples.

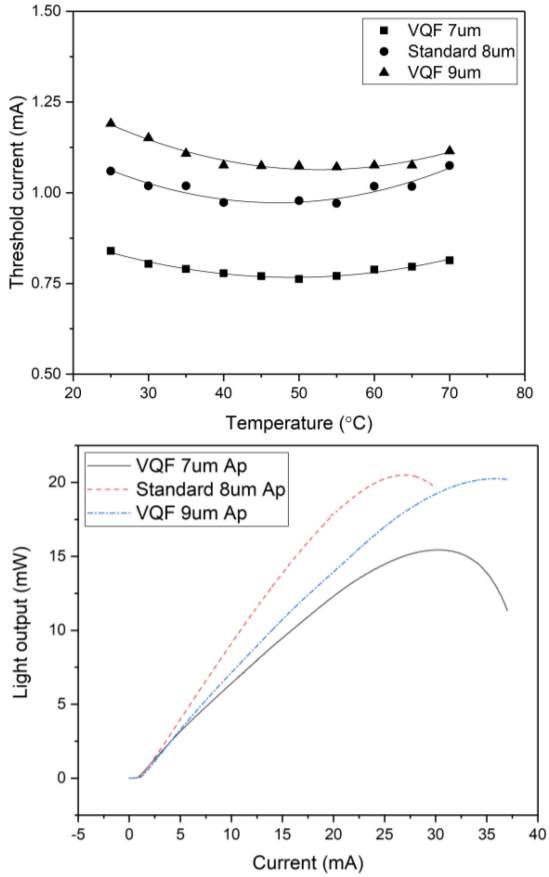

Fig. 5. Temperature dependence of the threshold current fitted with a second order polynomial (top) and L-I characteristic at room temperature up to thermal rollover (bottom) for VQF and Standard VCSEL devices.

The typical output optical power-current (L-I) characteristics of the standard and VQF device types, measured up to thermal rollover are shown in Fig. 5 (bottom). In general, the maximum output power is higher for the standard VCSELs, with some 8 μm aperture devices reaching up to 27.5 mW. However, the onset of thermal rollover occurs at significantly lower currents than for the VQF devices (up to 10 mA for a given aperture diameter), which can be seen in Fig. 5, and, again, is a result of a difference in electrical and thermal impedance. We extract the power conversion efficiency, η_{pow}, at a fixed current of 6 mA and find that this is highest for the standard devices, although there is good agreement for the maximum power conversion efficiency at $\sim$30%, but again occurring at lower currents for standard devices. The mean η_{pow} for a 7 and 8 μm VQF and standard VCSEL is measured as 30.2 $\pm$ 4.2 and 32.5 $\pm$ 5.9%, respectively, with the error given by the standard deviation. The mean current corresponding to $\eta_{pow,max}$ is then observed to be 3.5 $\pm$ 0.7 and 5.0 $\pm$ 0.4 mA for a 7 and 8 μm aperture standard and VQF device. The slope efficiency, η_{ext}, measured between 5 and 10 mA is consistently higher for the standard VCSELs, with a value of 0.89 W/A for an 8 μm aperture standard device, compared to 0.65 and 0.77 W/A for a 7 and 9 μm aperture VQF device, respectively. The reduction in η_{ext} of the VQF device compared to the standard VCSEL design is consistent with a higher rate of non-radiative recombination away from the lasing

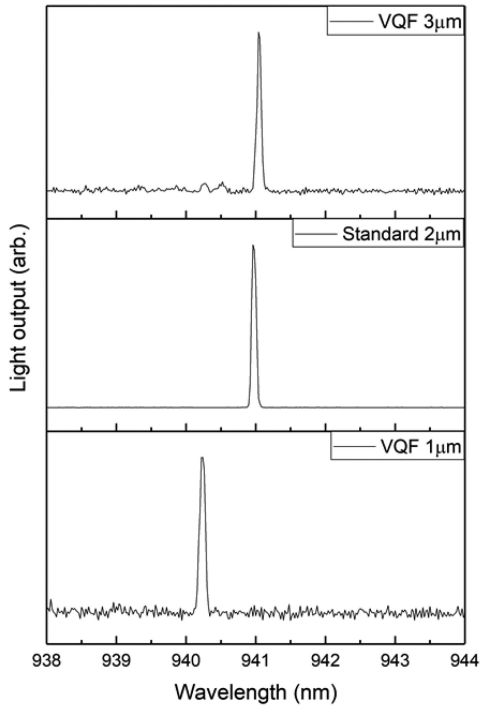

Fig. 6. Single-mode emission spectra for oxide aperture diameters < 3 μm.

mode, that is, where the carrier density is not pinned, which is likely driven by surface recombination at the exposed mesa sidewalls of the VQF designs.

Single mode emission for oxide aperture diameters < 3 μm up to 2 mA injection current is achieved in VQF devices, the spectra for which are shown in Fig. 6. The emission spectra for devices produced by VQF are comparable to that of standard device structures. Further, the number of lasing modes in larger aperture devices are also comparable, shown in the multi-mode spectra in Fig. 7. However, we do observe the wavelength of the fundamental mode to be redshifted in the standard VCSELs, which we attribute to temperature effects driven by additional Joule heating associated with the increased thermal impedance.

The redshift of the fundamental mode wavelength in the standard VCSELs is seen more clearly in the 8 μm aperture device in Fig. 8, where the extracted wavelengths for all devices measured are plotted. The cavity resonance wavelength extracted from post-growth reflectometry measurements is shown by the dashed line corresponding to a value of 941.4 nm for both device types. We see by considering the mean values that, in general, the standard VCSEL devices are more redshifted relative to the material cavity resonance wavelength, indicative of greater self-heating. The current-tuning redshift of the lasing wavelength of an 8 μm aperture standard and 9 μm aperture VQF device is measured as 0.51 and 0.08 nm/mA, respectively. From this, an estimated temperature increase per unit current is calculated by dividing these quantities by the measured temperature dependence of the lasing wavelength (0.07 nm/K). This gives a temperature shift, ΔT, of 7.2 and 1.1 K/mA for the standard and VQF devices, respectively. Hence, it is expected that the internal temperature of a standard VCSEL is higher than that of a VQF VCSEL for a given active area and at a fixed current.

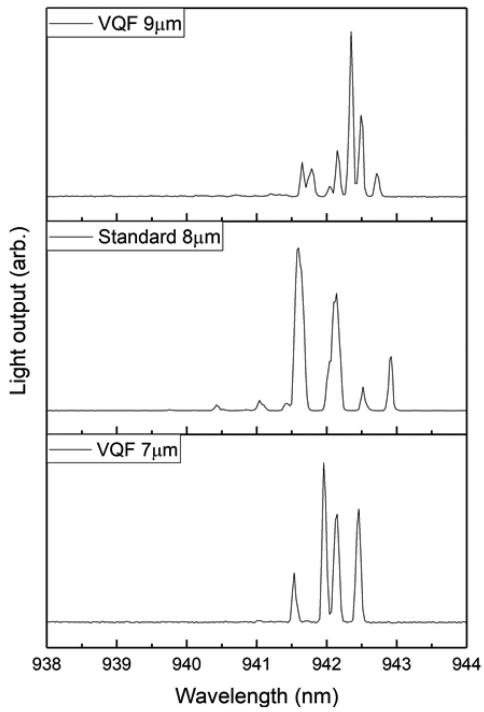

Fig. 7. Multi-mode emission spectra for devices of oxide apertures 7-9 μm diameter.

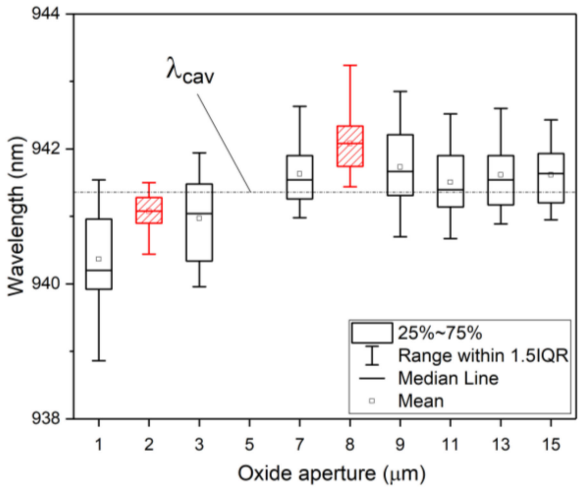

Fig. 8. Box and whisker plots for the measured fundamental mode wavelengths of VQF (plain boxes) and standard (striped boxes) VCSEL devices.

Here, it has been demonstrated that the performance of VQF VCSELs is representative of standard devices and that the observed disparities can be explained by consideration of device thermal properties, and the limitations imposed by the unpassivated mesa sidewalls and non-circular aperture shape. The difference in room temperature threshold current is understood by considering the temperature dependent gain peak-to-cavity resonance detuning and the difference in threshold lasing wavelength by comparing the difference in operating temperatures at a given current driven by the thermal impedances. We have also identified that an enhanced rate of surface recombination in the VQF structures limits the best achievable threshold current and slope efficiency, but this effect is small and does not affect the aim of VQF which is the feedback to growth conditions and, hence, is principally concerned with relative uniformities within individual wafers and between growth runs.

The key quantities discussed and used to compare VQF and standard device performance are summarised in Table I.

A. On-Wafer VQF Performance

The fabrication and characterisation of VQF devices is a powerful tool that can be exploited to measure and assess the quality, uniformity, and reproducibility of VCSEL epitaxial material in a volume manufacturing environment. Using the on-tile performance characteristics analysed in the previous section, it is possible to gain insight into the origins of epitaxial variations on the wafer-scale. However, the fabrication of large diameter wafers inherently introduces non-uniformity due to the fabrication process, and thus, to confidently assess the epitaxial material quality, the effects that are related to material growth and those due to device fabrication must be disentangled.

One of the most useful wafer characterisation techniques currently used is the measurement of the reflectivity spectrum of the VCSEL material at many locations across the wafer, and, from the resulting spectra, extraction of the cavity resonance wavelength, λ_{cav}. This allows the expected lasing wavelength to be mapped across a wafer. In Fig. 9 (top), a wafer-map of the cavity resonance wavelength, λ_{cav}, is shown, and in Fig. 9 (bottom), this is compared with measurements of the lasing wavelength, λ_0 from VQF devices along a horizontal line-profile. The spatial variation trend of the emission wavelength matches well with that of the material cavity. However, a redshift relative to λ_{cav} is observed and is consistent with self-heating caused by electrical pumping. Additionally, it is also be observed that the number of lasing modes for a given mesa size varies with a similar trend across the wafer, suggestive of a non-uniformity in active area defined by the oxide aperture.

To confirm this, the oxidation length, which was monitored during fabrication, is plotted against position on the wafer. The oxidation length is found to be greatest at the edge, resulting in a reduction in oxide aperture diameter approximately radially. Subsequently, the true VCSEL oxide aperture and thus active area of devices at the centre and edge of the wafer are, in reality, quite different. This causes a significant variation in important device performance parameters such as series resistance (thus any associated Joule heating), the lasing wavelength and the number of lasing modes observed, as well as the threshold current. The radial variation in oxidation length measured for a 38 μm mesa VQF device and the corresponding series resistance is shown in Fig. 10.

To understand the origin of the oxidation non-uniformity the oxidation extent of simple cylindrical mesa structures on tile samples cleaved from the centre and edge of a nominally identical 6-inch wafer were measured. For these samples, which underwent the same thermal oxidation process with both placed in the centre of the furnace, the oxidation rate is found to be slower for the sample taken from the edge of the wafer in comparison to the centre - opposite to the result observed

TABLE I
COMPARISON OF KEY DEVICE CHARACTERISTICS FOR VQF AND STANDARD VCSELS. INCLUDED ARE QUANTITIES FOR MESA DIAMETER, OXIDE APERTURE DIAMETER, MEAN SERIES RESISTANCE (R), THRESHOLD CURRENT (I_{th}), THRESHOLD CURRENT DENSITY (J_{th}), TEMPERATURE SHIFT DUE TO JOULE HEATING (ΔT), TEMPERATURE CORRESPONDING TO GAIN PEAK CAVITY RESONANCE ALIGNMENT (T_{min}), THRESHOLD CURRENT MINIMUM (α), MAXIMUM POWER CONVERSION EFFICIENCY AND SLOPE EFFICIENCY AT 6 mA (η_{ext})

Device	Mesa(μm)	Aperture (μm)	R (Ω)	I_{th} (mA)	J_{th} (kA/cm^2)	ΔT (°C/mA)	T_{min} (°C)	α (mA)	η_{pow} (%)	η_{ext} (W/A)
VQF	34	7	56.0	1.2	2.2	1.1	49.2	0.77	28.2	0.65
Standard	26	8	77.2	1.0	2.0	7.2	47.4	0.97	36.4	0.89
VQF	36	9	45.0	0.8	1.8	1.1	53.2	1.44	32.7	0.77

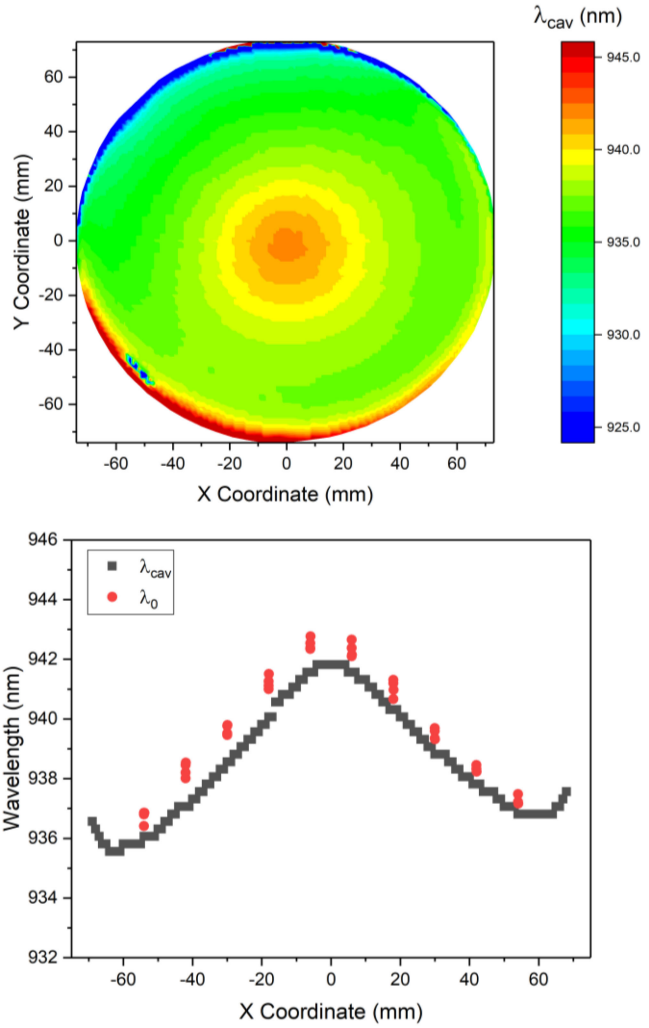

Fig. 9. Wafer map of material cavity resonance wavelength (top) and comparison of these values to measured lasing wavelengths along a horizontal line profile (bottom).

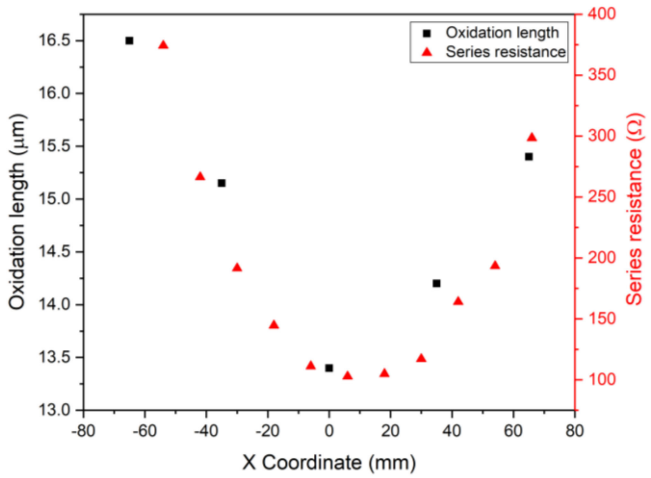

Fig. 10. Radial variation of oxidation length and series resistance measured at 1.8 V for a 38 μm VQF device.

when oxidising a full 6-inch wafer. For the cleaved tiles this result implies the edge-to-centre oxidation variation is driven by non-uniformity in the wafer epitaxial layers, such as variation in the composition or layer thickness of the high Al content layer in the top DBR, rather than being a fabrication induced non-uniformity [30], [31]. For full wafer processing, where the opposite non-uniformity trend is observed, this is attributed to the strain-induced wafer-bow associated with growth on GaAs substrates. This alters the thermal contact of the wafer to the heated chuck in the oxidation furnace, which results in a decrease in substrate temperature of approximately 5 °C at the centre of the wafer during the thermal oxidation process. Due to the exponential dependence of the oxidation process on temperature, this centre-edge temperature gradient results in a significantly different oxidation rate, the effect of which is observed during full-wafer characterisation. The impact of the wafer bow on temperature and thus oxidation rate is so significant that it dominates the effect of the slower oxidation rate observed in edge material that was measured on tile samples. Therefore, the impact of the strain-induced wafer bow cannot be ignored for large diameter processing of VCSEL epi-structures on GaAs, and corrections are needed to maximise fabrication tolerances and device yield. This is particularly an issue for furnaces where temperature control relies on thermal contact with the heated chuck. It has been shown that VCSEL structures can be grown on Ge substrates and, owing to the elemental nature of Ge, these wafers exhibit virtually no bowing [32]. Thus, growth on Ge is promising for improving manufacturing yield of VCSELs.

The impact of the oxidation non-uniformity can be seen in the spatial variation of threshold current for 38 μm mesa VQF VCSELs, shown in Fig. 11 (top). For these equivalent mesa diameters, the values decrease at the edge of the wafer, which is in agreement with a reduction in the diameter of the oxide defined VCSEL aperture area. This centre-to-edge variation for this mesa size is $\sim$1 mA, however, given the oxidation length variation, equivalent mesa diameters do not yield equivalent oxide aperture diameters. The effects of the known variation in aperture diameter can be accounted and corrected for by

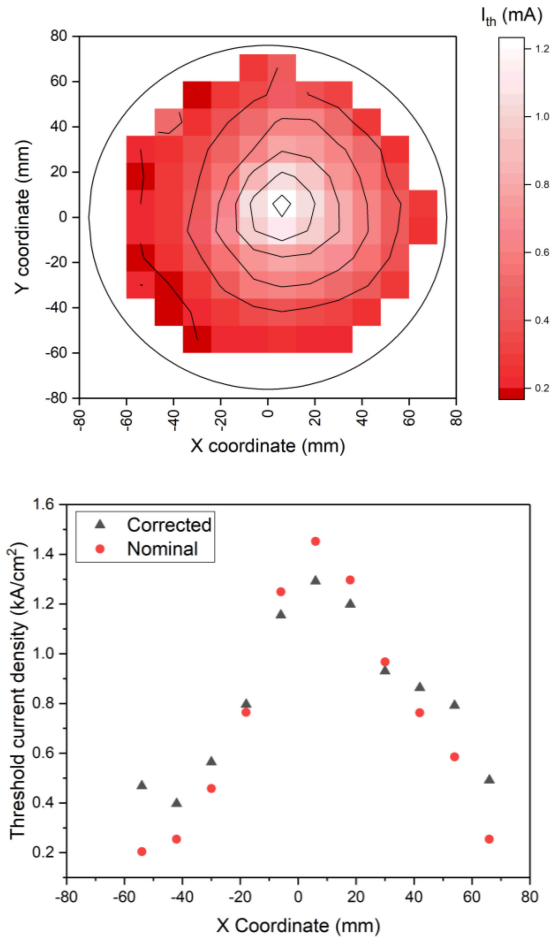

Fig. 11. Spatial variation of threshold current for 38 μm mesa devices (top) and threshold current density for nominal and corrected aperture diameters (bottom).

mapping the threshold current density, J_{th} rather than threshold current, I_{th}. A line scan at Y $= -6$ mm of J_{th} is shown in Fig. 11 (bottom), where the true spatial variation in room temperature threshold current density can be seen after correction for the $\sim$3 μm centre-to-edge oxidation length variation. Although, even after correction, significant variation in the centre-to-edge values for J_{th} remains, with a magnitude of 0.9 kA/cm^2, which is attributed to epitaxial growth non-uniformity, affecting for example, gain peak-to-cavity resonance detuning, and temperature effects.

With direct oxidation rate effects removed, the effects due to differences in operating temperature can be quantified. As shown previously, in Fig. 5 (top), increased operating temperatures result in a reduction in J_{th} for $T < T_{min}$. By extracting the threshold current from the L-I characteristic between 25 and 70 °C, the temperature corresponding to the gain peak-to-cavity resonance alignment, T_{min}, was spatially mapped on the wafer.

Spatial variations in the epi-layers across the VCSEL wafer affect the gain peak-to-cavity resonance detuning, and hence impact the threshold current density. Non-uniformities in the thickness and composition of the inner cavity layers impact the cavity resonance wavelength. Likewise, these non-uniformities in the QW layers affect the gain spectrum and, in combination, the detuning, $\Delta\lambda$. Therefore, it is expected that some variation

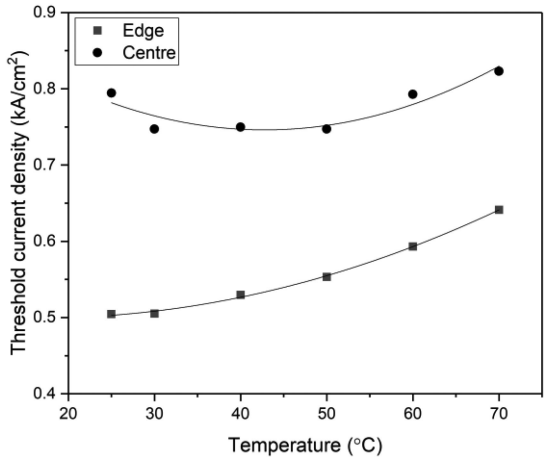

Fig. 12. Temperature dependence of threshold current for 12.5 μm aperture devices measured at the edge and centre of a 6-inch wafer.

in T_{min} will be observed owing to a spatial variation in the detuning across the wafer, and, hence, at a given temperature, there will be a spatial variation in threshold current density, a component of which is driven by the detuning. We find that T_{min} is highest in the centre of the wafer at an ambient temperature of 45-50 °C, and lowest at the edge at around 20-25 °C, this is evident in Fig. 12 in the plot of J_{th} versus temperature. This reveals that, at room temperature, the degree of detuning is greatest in the centre of the wafer. Using the temperature dependence of the cavity resonance wavelength (0.07 nm/K), the detuning is calculated as 1.4 nm in the centre and is found to be zero for edge devices. It should be noted, though, that the reduction in aperture diameter towards the edge, associated with the increased oxidation length for a bowed GaAs wafer, results in an increase in device thermal impedance, and this means that the internal temperature of the VQF device, with a fixed active area and at a given current, shifts higher at the edge. Therefore, the spatial variation in the magnitude of the gain peak-to-cavity resonance detuning is not as large as that given by the calculation employing $T_{\min}$, that is, the difference of 1.4 nm between the centre and edge is an upper limit on the actual value of $\Delta\lambda$. The measurement of the gain peak-to-cavity resonance detuning is an important result for VQF processing and provides an insight that is not directly observable with standard wafer characterisation techniques used to assess epitaxy against target specification. Quantifying the variation of $\Delta\lambda$ and T_{min} across large diameter wafers allows an assessment of device yield at elevated temperatures which is critical for most VCSEL applications, and which is not otherwise possible to measure.

Further, and significantly, the observation that at ambient room temperature the gain peak and cavity resonance are in alignment at the edge of the wafer, means devices operate close to the minimum in threshold current (density). Therefore, consideration of the spatial variation in I_{th} or J_{th} at room temperature ignores any influence of the gain peak-to-cavity resonance detuning, which must be accounted for to provide a full picture of the insights gained by VQF. Due to the temperature dependence of I_{th} and the spatial variation of T_{min}, the observed

difference in threshold current at different regions of the wafer also varies as a function of temperature.

In Fig. 12, it is evident that the centre-to-edge variation reduces as the ambient temperature is increased. Many VCSEL applications require operation at elevated temperatures, hence measurement of only the room temperature performance is insufficient. As for in section A, from the temperature dependence of I_{th}, the threshold current (density) minimum is extracted. This is found to be lowest at the wafer edge, which is also evident in Fig. 12. So, not only is the room temperature threshold current density lowest at the edge of the wafer, the minimum in threshold current density, $J_{th,min}$, corresponding to the alignment of the gain peak and cavity resonance wavelength is also lower. Therefore, even with the detuning working to decrease J_{th} at the edge, the minimum achievable J_{th} is lower at the edge as well, and this result is attributed to variation of the epitaxial layers. In comparing $J_{th,min}$, we find that the centre-to-edge variation decreases again to $\sim$0.3 kA/cm^2. Hence with the consideration of $J_{th,min}$ the effects of variation due to fabrication (oxidation) and temperature (detuning) are excluded, and the residual variation reflects the material only. However, although $J_{th,min}$ represents an important figure of merit for the VCSEL, it is more useful to consider the spatial variation at temperatures of interest. In commercialised applications, 940 nm VCSELs are often intended for operation at 50 °C ambient temperature. At this temperature, it is found that the centre-to-edge variation in J_{th} is further reduced to $\sim$0.2 kA/cm^2. Hence, the yield of VQF devices, and, more specifically, the percentage of the epi-wafer which produces devices that meet the requirements of the design specification, would be seen to dramatically increase after observing the performance at an elevated temperature, closer to the conditions of intended application, compared to room temperature characterisation only.

With these experimental results it has been shown that the VQF process produces VCSEL devices that are representative of standard VCSEL performance, in a fraction of the time usually required. The application of VQF to full wafers has been demonstrated to provide valuable information on the quality and yield of epitaxial material, with insights that are not possible to obtain with typical material characterisation methods employed during the production process.

IV. Conclusion

In summary, the applicability of a stripped-back VCSEL Quick Fabrication (VQF) process to the prediction of standard VCSEL performance has been demonstrated. Full wafer processing of VQF devices has been shown to provide valuable insight into epitaxial material variation, with $\sim$60% reduction in fabrication time, yielding valuable insights which cannot be obtained through traditional material characterisation techniques. While here the VQF technique has been demonstrated on generic 940 nm emission wavelength material, its utility in characterising key parameters, such as threshold current behaviour and gain peak-to-cavity resonance detuning, is similarly applicable to VCSEL epi-material designed for different wavelengths and final applications. Hence, this process will provide great benefits in industry as a regular practise of quality control, in tracking drift in a growth campaign and for providing feedback to growth conditions to optimise epitaxial material quality and maximise yield.

Acknowledgment

Due to confidentiality agreements with research collaborators, supporting data can only be made available to bona fide researchers subject to a non-disclosure agreement. Details of the data and how to request access are available at the Cardiff University Research Data Archive at http://doi.org/10.17035/d.2022.0176629008.

References

[1] D. L. Huffaker, D. G. Deppe, K. Kumar, and T. J. Rogers, "Native-oxide defined ring contact for low threshold vertical-cavity lasers," *Appl. Phys. Lett*, vol. 65, 1994, Art. no. 97, doi: 10.1063/1.113087.

[2] K. D. Choquette, K. L. Lear, R. P. Schneider, and K. M. Geib, "Cavity characteristics of selectively oxidized vertical-cavity lasers," *Appl. Phys. Lett*, vol. 66, 1995, Art. no. 3413, doi: 10.1063/1.113371.

[3] K. D. Choquette, K. M. Geib, H. Q. Hou, D. Mathes, and R. Hull, "Technology and applications of selective oxidation of AlGaAs," in *Proc. IEEE Semicond. Semi-Insulating Mater. Conf. SIMC*, 1999, pp. 209–213, doi: 10.1109/SIM.1998.785109.

[4] R. S. Geels, S. W. Corzine, J. W. Scott, D. B. Young, and L. A. Coldren, "Low threshold planarized vertical-cavity surface-emitting lasers," *IEEE Photon. Technol. Lett.*, vol. 2, no. 4, pp. 234–236, Apr. 1990, doi: 10.1109/68.53246.

[5] J. L. Jewell, J. P. Harbison, A. Scherer, Y. H. Lee, and L. T. Florez, "Vertical-Cavity surface-emitting lasers: Design, growth, fabrication, characterization," *IEEE J. Quantum Electron.*, vol. 27, no. 6, pp. 1332–1346, Jun. 1991, doi: 10.1109/3.89950.

[6] T. Tanigawa, T. Onishi, S. Nagai, and T. Ueda, "12.5-Gbps operation of 850-nm vertical-cavity surface-emitting lasers with reduced parasitic capacitance by BCB planarization technique," *IEEE J. Quantum Electron.*, vol. 42, no. 8, pp. 785–790, Aug. 2006, doi: 10.1109/JQE.2006.878186.

[7] L. Marigo-Lombart *et al.*, "Self-aligned BCB planarization method for high-frequency signal injection in a VCSEL with an integrated modulator," *Semicond. Laser Dyn. VII, Proc. SPIE*, vol. 9892, pp. 272–280, Apr. 2016, doi: 10.1117/12.2227529.

[8] G. Giaretta, M. Y. Li, G. S. Li, W. Yuen, and C. J. Chang-Hasnain, "A novel 4 × 8 single-mode independently addressable oxide-isolated VCSEL array," *IEEE Photon. Technol. Lett.*, vol. 9, no. 9, pp. 1196–1198, Sep. 1997, doi: 10.1109/68.618475.

[9] C. L. Chua, R. L. Thornton, and D. W. Treat, "Planar laterally oxidized vertical-cavity lasers for low-threshold high-density top-surface-emitting arrays," *IEEE Photon. Technol. Lett.*, vol. 9, no. 8, pp. 1060–1062, Aug. 1997, doi: 10.1109/68.605499.

[10] K. M. Geib, K. D. Choquette, A. A. Allerman, R. D. Briggs, and J. J. Hindi, "Comparison of fabrication approaches for selectively oxidized VCSEL arrays," in *Proc. Vertical-Cavity Surf.-Emitting Lasers IV*, May 2000, vol. 3946, pp. 36–40, doi: 10.1117/12.384385.

[11] C. L. Chua, R. L. Thornton, D. W. Treat, and R. M. Donaldson, "Independently addressable VCSEL arrays on 3-μm pitch," *IEEE Photon. Technol. Lett.*, vol. 10, no. 7, pp. 917–919, Jul. 1998, doi: 10.1109/68.681269.

[12] Y. Hao *et al.*, "Optimal design for improving performance of VCSELs," in *Proc. Acad. Symp. Optoelectron.Microelectron. Technol. 10th Chin.-Russian Symp. Laser Phys. Laser Technol. RCSLPLT/ASOT*, 2010, pp. 93–95, doi: 10.1109/RCSLPLT.2010.5615393.

[13] R. Michalzik, "VCSEL fundamentals," in *Springer Series in Optical Sciences*, vol. 166, Berlin, Heidelberg, USA: Springer, 2012, doi: 10.1007/978-3-642-24986-0_2.

[14] T. Flick, K. H. Becks, J. Dopke, P. Mättig, and P. Tepel, "Measurement of the thermal resistance of VCSEL devices," *J. Instrum.*, vol. 6, no. 1, Jan. 2011, Art. no. C01021, doi: 10.1088/1748-0221/6/01/C01021.

[15] M. Xun *et al.*, "Analysis of thermal properties of 940-nm vertical cavity surface emitting laser arrays," *IEEE Trans. Electron Devices*, vol. 68, no. 1, pp. 158–163, Jan. 2021, doi: 10.1109/TED.2020.3039934.

[16] B. J. Thibeault *et al.*, "Evaluating the effects of optical and carrier losses in etched-post vertical cavity lasers," *J. Appl. Phys.*, vol. 78, no. 10, pp. 5871–5875, Nov. 1995, doi: 10.1063/1.360588.

[17] E. R. Hegblom, D. I. Babic, B. J. Thibeault, and L. A. Coldren, "Scattering losses from dielectric apertures in vertical-cavity lasers," *IEEE J. Sel. Top. Quantum Electron.*, vol. 3, no. 2, pp. 379–389, Apr. 1997, doi: 10.1109/2944.605682.

[18] K. D. Choquette, W. W. Chow, G. R. Hadley, H. Q. Hou, and K. M. Geib, "Scalability of small-aperture selectively oxidized vertical cavity lasers," *Appl. Phys. Lett.*, vol. 70, no. 7, pp. 823–825, Feb. 1997, doi: 10.1063/1.118234.

[19] L. A. Coldren, S. W. Corzine, and M. Mashanovitch, "Gain and current relations," in *Diode Lasers and Photonic Integrated Circuits*. L. A. Coldren, S. W. Corzine and M. L. Mašanović Eds., Hoboken, NJ, USA: Wiley, 2012, doi: 10.1117/1.601191.

[20] D. Naidu, "Characterisation of lateral carrier out-diffusion and surface recombination in ridge waveguide devices," Ph.D. thesis, Cardiff Univ., 2009. [Online]. Available: http://orca.cardiff.ac.uk/id/eprint/54892

[21] P. Blood, "Temperature dependence of threshold current," in *Quantum Confined Laser Devices: Optical Gain and Recombination in Semiconductors*. Oxford, U.K.: Oxford Univ. Press, Oct. 2015, doi: 10.1093/acprof:oso/9780199644513.001.0001.

[22] J. Talghader and J. S. Smith, "Thermal dependence of the refractive index of GaAs and AlAs measured using semiconductor multilayer optical cavities," *Appl. Phys. Lett.*, vol. 66, no. 3, pp. 335–337, Jan. 1995, doi: 10.1063/1.114204.

[23] M. B. Panish and H. C. Casey, "Temperature dependence of the energy GaP in GaAs and GaP," *J. Appl. Phys.*, vol. 40, 1969, Art. no. 163, doi: 10.1063/1.1657024.

[24] K. D. Croquette and H. Q. Hou, "Vertical-cavity surface emitting lasers: Moving from research to manufacturing," *Proc. IEEE*, vol. 85, no. 11, pp. 1730–1739, Nov. 1997, doi: 10.1109/5.649649.

[25] H. Li *et al.*, "Impact of the quantum well gain-to-cavity etalon wavelength offset on the high temperature performance of high bit rate 980-nm VCSELs," *IEEE J. Quantum Electron.*, vol. 50, no. 8, pp. 613–621, Aug. 2014, doi: 10.1109/JQE.2014.2330255.

[26] N. I. Khan, S. H. Choudhury, and A. A. Roni, "A comparative study of the temperature dependence of lasing wavelength of conventional edge emitting stripe laser and vertical cavity surface emitting laser," in *Proc. Int. Conf. Opt. Commun. Syst.*, 2011, pp. 1–5, doi: 10.5220/0003512101410145.

[27] C. Chen, P. O. Leisher, A. A. Allerman, K. M. Geib, and K. D. Choquette, "Temperature analysis of threshold current in infrared vertical-cavity surface-emitting lasers," *IEEE J. Quantum Electron.*, vol. 42, no. 10, pp. 1078–1083, Oct. 2006, doi: 10.1109/JQE.2006.881828.

[28] M. Ogura and H. C. Hsieh, "Effect of surface recombination velocity on the threshold current and differential quantum efficiency of the surface-emitting laser diode," *IEEE J. Quantum Electron.*, vol. 32, no. 4, pp. 597–606, Apr. 1996, doi: 10.1109/3.488832.

[29] G. M. Yang, M. H. MacDougal, V. Pudikov, and P. D. Dapkus, "Influence of mirror reflectivity on laser performance of very-low-threshold vertical-cavity surface-emitting lasers," *IEEE Photon. Technol. Lett.*, vol. 7, no. 11, pp. 1228–1230, Nov. 1995, doi: 10.1109/68.473454.

[30] K. D. Choquette *et al.*, "Advances in selective wet oxidation of AlGaAs alloys," *IEEE J. Sel. Top. Quantum Electron.*, vol. 3, no. 3, pp. 916–925, Jun. 1997, doi: 10.1109/2944.640645.

[31] K. M. Geib, K. D. Choquette, H. Q. Hou, and B. E. Hammons, "Fabrication issues of oxide-confined VCSELs," in *Proc. Vertical-Cavity Surf.-Emitting Lasers*, Apr. 1997, vol. 3003, pp. 69–74, doi: 10.1117/12.271054.

[32] A. Johnson *et al.*, "High performance 940nm VCSELs on large area germanium substrates: The ideal substrate for volume manufacture," in *Proc. SPIE Vertical-Cavity Surface-Emitting Lasers XXV*, 2021, Art. no. 1170404, doi: 10.1117/12.2583207.